Summer 2020

ARTFIMA processes and their applications to solar flare data

Jinu Kabala
Iowa State University

ARTFIMA processes and their applications to solar flare data

by

Jinu Susan Kabala

A Creative Component submitted to the graduate faculty

in partial fulfillment of the requirements for the degree of

MASTER OF SCIENCE

Major: Statistics

Program of Study Committee:
Farzad Sabzikar, Major Professor
Daniel Nordman
Ananda Weerasinghe

Iowa State University

Ames, Iowa

2020

TABLE OF CONTENTS

Page

LIST OF TABLES

Page

LIST OF FIGURES

Page

ABSTRACT

In this work, we demonstrate the application of ARTFIMA models on stable data derived from solar flare soft x-ray emissions. We study the solar flare data during a period of solar minimum which occurred most recently in July, August and September 2017. We use a two-state Hidden Markov Model to extract shorter stationary trajectories from the solar flare time series and classifying it into two states. In this work, we also introduce the ARTFIMA-GARCH model to model some of the trajectories. We do an end-to-end analysis, modeling and prediction of the solar flare data using both ARFIMA and ARTFIMA-GARCH models. We show through visual inspection and statistical tests that the models fit using ARTFIMA and the ARTFIMA-GARCH models describe the data better than the ARFIMA and ARFIMA-GARCH models which is the state of the art approach to model this data.

CHAPTER 1. INTRODUCTION

The autoregressive tempered fractionally integrated moving average (ARTFIMA) time series model which is a tempered fractionally integrated time series that exhibit semi-long range dependence due to the behavior of its covariance function [1]. The ARTFIMA model is an important model to consider when modelling data that is traditionally modeled by the ARFIMA model. This is due to the following ways in which ARTFIMA distinguishes from an ARFIMA model which is not a tempered time series. Firstly, the ARFIMA model is stationary only when the long memory paramter $|d| < 0.5$ whereas the ARTFIMA model is stationary when $d \in \mathcal{R} \setminus \mathcal{Z}^{-}$. Secondly, the ARTFIMA model has a covariance function that is absolutely summable, which makes it easier to analyze. It has also been shown that the ARTFIMA model [1, 2] performs better than the ARFIMA models in many applications spanning climate, stock returns, water turbulence, and hydrology under the assumption of finite error variance.

However, certain applications are best modeled by distributions that exhibit infinite variance. A stable distribution is an infinite-variance distribution of special significance as it is the limiting distribution of normalized sum of independent identically distributed random variables, which is closed under convolution. Stock market prices and telephone noise have been modeled as a large sum of such random variable [3]. For the distribution of stock price changes, a stable Paretian distribution has been used [4]. Another noteworthy application is in signal processing [5]. The ARFIMA model with stable skewed innovations have been applied to describe the movement of mRNA molecules in E.coli cells [6]. Recently, a stable ARFIMA process has been used to model UMTS data [7].

In the field of astronomy, a popular data set that exhibits infinite variance is the solar flare data [8]. The sun emit strong X-rays which are measured by satellites. The launch of satellites like the Geostationary Operational Environmental Satellite (GOES) [9] by the National Oceanic

and Atmospheric Administration (NOAA) [10] has enabled the continuous measurement of solar X-ray emissions. Such measurements are available since 1974. The solar cycle happens periodically every 11 years when the sun moves through a period of solar minimum which is marked by fewer and smaller flares to a period of solar maximum marked by more prominent flares. Studying the variability of solar flares as well as its prediction is an important problem in solar physics. Changes in solar activity can affect space weather and pose threats to man-made spacecrafts, and disrupt power-grids and satellite communication channels like GPS. The ARFIMA time series model has been widely applied to the study of soft X-ray emissions [8, 11]. In [8], the FARIMA model with Pareto noise was used to predict solar flare soft X-ray emissions in the period of solar maxima. This FARIMA model was used to study data since 1978 which spanned three solar cycles since the launch of the GOES satellities. In a recent paper [11], the analysis of a period of solar minimum was studied for the period July-September 2017 using ARFIMA and ARFIMA-GARCH models. The paper used a two state approach to distinguish the flare activity to choose the appropriate model.

In this work, we study the same problem as [11] which applies different statistical models to analyze, model and predict soft X-ray solar emission activity during a period of solar minimum. We use the same data-set from NOAA for the months of July, August and September 2017 that is separated into two states. During these months, the sun was approaching the solar minimum which is the minimum of the next solar cycle that happens every 11 years.

1.1 Contributions

We make three main contributions in this work.

- The ARTFIMA model has been applied to various datasets [1, 2] to model climate, stock returns, water turbulence, and hydrology under the assumption of finite error variance. We demonstrate the application of the ARTFIMA model with stable innovations on solar X-ray emissions data. We show that whittle estimation can be used to estimate the parameters of the ARTFIMA process with stable innovations. [2].

- We also introduce the ARTFIMA-GARCH model by fitting the model on some trajectories of the solar X-ray emission data. This is the first application of the composite ARTFIMA-GARCH process to any dataset.

- We compare the performance of ARTFIMA and ARTFIMA-GARCH model with the ARFIMA and ARFIMA-GARCH models on the different trajectories of soft solar flare data. We show through rigorous statistical analysis that the ARTFIMA and ARTFIMA-GARCH models fit the solar flare data better, and can be useful to make future predictions more accurately. This improvement over ARFIMA and ARFIMA-GARCH is primarily due to the effect of tempering in the ARTFIMA and ARTFIMA-GARCH models. Due to this tempering effect, the spectral density of the ARTFIMA model fits the data periodogram better than the ARFIMA spectral density. For trajectories that have a long memory paramter, $d > 0.5$, the ARFIMA and ARFIMA-GARCH models are misspecified as the model is non-stationary when $d > 0.5$.

1.2 Organization of work

In Chapter 2, we provide a background of the ARTFIMA model with stable innovations along with details of parameter estimation. In this chapter, we also define the ARTFIMA-GARCH model and provide the spectral density. In Chapter 3, we apply both ARTFIMA and ARTFIMA-GARCH models to the solar flare data and compare it to ARFIMA and ARFIMA-GARCH models. The chapter explains in detail using visual plots and rigorous statistical analysis the preferred choice of model for the specific trajectory of solar flare data. The chapter concludes with analyzing the accuracy of the proposed model to make future predictions of the solar flare data. We provide a summary and discussion in Chapter 4.

CHAPTER 2. MODEL BACKGROUND

In this chapter, we give a brief background to ARTFIMA and ARTFIMA-GARCH models. In Section 2.1, we define the ARTFIMA model and describe the parameter estimation method used in the stable innovation case. We also define the co-difference for the stable ARTFIMA process and define the spectral density for the finite variance case. In Section 2.2, we define the ARTFIMA-GARCH model and describe the spectral density under the finite variance assumption.

2.1 ARTFIMA Process

The ARTFIMA model when the innovations have finite variance, was introduced in [2]. In this section, we define the ARTFIMA model with infinite variance innovations and provide essential facts including causality, invertibility, and the codifference structure. The tempered fractional difference operator is defined by:

$$\Delta^{d,\lambda} f(x) = (I - e^{-\lambda} B)^d f(x) = \sum_{j=0}^{\infty} \omega_{d,\lambda}(j) f(x-j) \tag{2.1}$$

where $d > 0$, $\lambda > 0$, $BX_t = X_{t-1}$ is the backward shift operator, and

$$\omega_{d,\lambda}(j) := \frac{\Gamma(j-d)}{\Gamma(j+1)\Gamma(-d)} e^{-\lambda j} \tag{2.2}$$

using the gamma function $\Gamma(d) = \int_0^\infty e^{-x} x^{d-1}\, dx$. By applying the well-known property $\Gamma(d+1) = d\Gamma(d)$, we can extend (2.1) to non-integer values of $d < 0$. By a similar abuse of notation, we call this a tempered fractional integral. If $\lambda = 0$, then equation (2.1) reduces to the usual fractional difference operator, see [12, 13] for more details.

Next, we define the ARTFIMA model with infinite variance. The discrete time stochastic process $\{X_t\}_{t\in\mathbb{Z}}$ is called an *autoregressive tempered fractional integrated moving average* time series, denoted by ARTFIMA(p, d, λ, q), if $\{X_t\}_{t\in\mathbb{Z}}$ is a stationary solution with zero mean of the tempered

fractional difference equations

$$\Phi(B)\Delta^{d,\lambda}X_t = \Theta(B)Z_t, \tag{2.3}$$

where $\{Z_t\}_{t\in\mathbb{Z}}$ belongs to the domain attraction of an α-stable law, $Z_t \in D(\alpha)$, with $0 < \alpha < 2$. This means there exist some constants $k_1, k_2 \geq 0, k_1 + k_2 > 0$ such that $\lim_{x\to+\infty} x^{\alpha}\mathbb{P}(Z_t > x) = k_1$ and $\lim_{x\to-\infty} |x^{-\alpha}\mathbb{P}(z_t \leq x)| = k_2$. Moreover $\mathbb{E}[Z_t] = 0$. Here $\Phi(z) = 1 - \phi_1 z - \phi_2 z^2 - \ldots - \phi_p z^p$, and $\Theta(z) = 1 + \theta_1 z + \theta_2 z^2 + \ldots + \theta_q z^q$ are polynomials of degrees $p, q \geq 0$ with no common zeros. It follows from (2.3) that X_t is ARTFIMA(p, d, λ, q) if and only if $Y_t = \Delta^{d,\lambda}X_t$ is an ARMA(p, q) time series

$$Y_t - \sum_{j=1}^{p} \phi_j Y_{t-j} = Z_t + \sum_{i=1}^{q} \theta_i Z_{t-i}$$

where $\{Z_t\}_{t\in\mathbb{Z}} \in D(\alpha)$. In this paper, we always assume the polynomials $\Phi(\cdot)$ and $\Theta(\cdot)$ have no common zeros and

$$\big|\Phi(z)\big| > 0 \quad \text{and} \quad \big|\Theta(z)\big| > 0 \tag{2.4}$$

for $|z| \leq 1$. Using (2.3), it can be shown that X_t has the moving average representation

$$X_t = \Delta^{-d,\lambda}\frac{\Theta(B)}{\Phi(B)}Z_t = \sum_{j=0}^{\infty} a_{-d,\lambda}(j)Z_{t-j}, \tag{2.5}$$

where $a_{-d,\lambda}(j)$ is given

$$a_{-d,\lambda}(j) = \sum_{s=0}^{j} \omega_{-d,\lambda}(s)b(j-s) \tag{2.6}$$

for $j \geq 0$ and the coefficients $b(j)$ obtained from $\Theta(z)\Phi(z)^{-1} = \sum_{j=0}^{\infty} b(j)z^j$. The time series $\{X_t\}$ is stationary for any $d \in \mathbb{R} \setminus \mathbb{Z}^-$ since $\sum_{j=0}^{\infty} |a_{-d,\lambda}(j)|^{\alpha} < \infty$ and this is in contrast with the ARFIMA(p, d, q) where we need to restrict $d < 1 - \frac{1}{\alpha}$ to have the stationary model. This fact is coming from the existence of the tempering exponential functional $e^{-\lambda k}$ in (2.5). Moreover, one can show that $\{X_t\}$ is invertible, see [2]. By assuming $Z_t \in D(\alpha)$ with $\alpha = 2$, we have $\mathbb{E}(Z_t^2) < \infty$ and hence we can compute the covariance function of this process. For the simplicity in the notations, assume $p = q = 0$. Then, the ARTFIMA model has a covariance function $\gamma(k) \sim Ce^{-\lambda k}k^{d-1}$ for large lags k, see [14]. Therefore, we say the ARTFIMA model X_t exhibit semi-long range dependence. This means that the covariance function exhibits long-range dependence for a certain

number of lags and then decays exponentially fast. If we let $Z_t \in D(\alpha)$ with $1 < \alpha < 2$ then the covariance function does not exist. Instead, another tool measurement which is called codifference can be used to describe the correlations between lags, see [15, 16, 17] for more details. The codifference is defined as follows:

$$\tau(X_0, X_k) = \ln \mathbb{E}^{i(X_k - X_0)} - \ln \mathbb{E}^{i(X_k)} \ln \mathbb{E}^{i(X_0)}. \tag{2.7}$$

For the ARTFIMA case with stable innovations, we have two possible cases: (i) If $(\alpha-1)(d-1) > -1$ then $\tau(X_0, X_k) \sim e^{-\lambda k} k^{\alpha(d-1)+1}$; (ii) If $(\alpha - 1)(d - 1) < -1$ then $\tau(X_0, X_k) \sim e^{-\lambda k} k^{d-1}$. In both cases, we see that codifference has two components, the power law and an exponential function which indicates the semi-long memory for the stable ARTFIMA process.

In order to understand the effect of tempering parameter λ we compare the spectral density functions of ARFIMA and ARTFIMA models. The spectral density of an ARTFIMA(p, d,λ, q) process $\{X_t\}$ defined in (2.3) satisfying (2.4) is defined as follows for the finite variance ARTFIMA process.

$$f_X(\nu) = \sigma^2 \frac{1}{2\pi} \frac{|\Theta(e^{-i\nu})|^2}{|\Phi(e^{-i\nu})|^2} |1 - e^{-(\lambda + i\nu)}|^{-2d} \tag{2.8}$$

for $-\pi \leq \nu \leq \pi$

Maximum likelihood estimation is used for an ARFIMA process with gaussian noise and whittle estimation is used for an ARFIMA stable noise process [18, 19]. The same applies to the ARTFIMA process as well. The maximum likelihood parameter estimation is well described in [2].

The whittle estimator Θ_0 of the parameter space $(\phi_1, ..., \phi_p, d, \lambda, \theta_1, ..., \theta_q)$ for a realization of an ARTFIMA process which has length N, is defined by:

$$\Theta_0 := \arg\min_{\Theta} \int_{-\pi}^{\pi} \frac{\mathcal{I}(\nu)}{\mathcal{K}(\nu, \theta)} d\nu \tag{2.9}$$

where the periodogram $\mathcal{I}(\nu)$ and scaled spectral density $\mathcal{K}(\nu, \theta)$ are defined as follows.

$$\mathcal{I}(\nu) = \frac{1}{2\pi N} |\sum_{t=1}^{N} X_t e^{it\nu}| \tag{2.10}$$

$$\mathcal{K}(\nu, \theta) = \frac{|\Theta(e^{-i\nu})|^2}{|\Phi(e^{-i\nu})|^2} |1 - e^{-(\lambda + i\nu)}|^{-2d} \tag{2.11}$$

Since $\sum_{j=-\infty}^{\infty} |a_j^{-d,\lambda}|^{\delta}|j| < \infty$, where $\delta = 1 \wedge \eta$, the proof for stable ARTFIMA parameter estimation using whittle estimator follows the proof in [20] holds.

2.2 ARTFIMA-GARCH Process

For the ARTFIMA models with finite variance, we assume identical innovations distributions with constant variance. A generalized autoregressive conditional heteroskedasticity (GARCH) model belongs to a class of models that have time varying conditional variance. The GARCH(k, l) model is defined for the process $\{Z_t\}$ as follows.

$$\begin{aligned} Z_t &= \sqrt{h_t}\eta_t \\ h_t &= \alpha_0 + \sum_{i=1}^{k} \alpha_i Z_{t-i}^2 + \sum_{j=1}^{l} \beta_j h_{t-j} \end{aligned} \tag{2.12}$$

where η_t is a sequence of i.i.d random variables.

We combine both ARTFIMA(p, d, λ, q) and GARCH(k, l) process and say that $\{X_t\}$ follows an ARTFIMA(p, d, λ, q)-GARCH(k, l) model when Z_t have finite second moments and satisfy Equation (2.12). A similar extension to an ARFIMA models exists called ARFIMA-GARCH [21, 22].

In this paper, we fit the residuals to an ARTFIMA(p, d,λ, q) - GARCH$(1, 1)$ model which is defined as follows:

$$\begin{aligned} &\Phi(B)(1 - e^{-\lambda}B)^d X_t = \Theta(B)Z_t \\ &Z_t = \sqrt{h_t}\eta_t \\ &h_t = \alpha_0 + \alpha_1 Z_{t-1}^2 + \beta_1 h_{t-1} \end{aligned}$$

The ARTFIMA model from Equation (2.3) describes the conditional mean and the GARCH model from Equation (2.12) describes the conditional variance of the process. The GARCH(1, 1) model satisfies second order stationarity only if $\alpha_1 + \beta_1 < 1$. Hence, the ARTFIMA(p, d,λ, q) - GARCH$(1, 1)$ model is stationary when all the roots of polynomials $\Phi(z)$ and $\Theta(z)$ lie outside the unit circle and $\alpha_1 + \beta_1 < 1$ for any $d \in \mathbb{R} \setminus \mathbb{Z}^-$ and $\lambda > 0$, the model is stationary . We know that ARFIMA(p,d,q) model and the ARFIMA(p,d,q)-GARCH(1,1) is stationary only if $-0.5 < d < 0.5$, but this condition doesn't hold for the ARTFIMA model [23].

We have seen the definition of the spectral density function of an ARTFIMA model in Section 2.1 and that of the ARFIMA model in [24]. The spectral density of an ARTFIMA(p, d,λ, q) - GARCH(1, 1) is given by the following.

$$f_X^*(\nu) = \sigma_Z^2 \frac{1}{2\pi} \frac{|\Theta(e^{-i\nu})|^2}{|\Phi(e^{-i\nu})|^2} |1 - e^{-(\lambda + i\nu)}|^{-2d} \tag{2.13}$$

$$\sigma_Z^2 = var(Z_t) = \frac{\alpha_0}{\alpha_1 + \beta_1} \tag{2.14}$$

We estimate the parameters of the composite ARTFIMA-GARCH process by first estimating the parameters of the ARTFIMA process using maximum likelihood or whittle estimation procedures based on the stability index α of the time series as described in Section 2.1. Next, we extract the residuals and estimate the parameters for the GARCH process using maximum likelihood estimation, the details of which are given in [25].

CHAPTER 3. AN APPLICATION TO SOLAR FLARE DATA

In this chapter, we apply the ARTFIMA and ARTFIMA-GARCH processes to the solar flare data. The steps taken to collect and preprocess the data is described in detail in Section 3.1. In Section 3.2, we estimate the long memory and stability parameters of the time series and describe the methods used to estimate them. We use these values to separate sub-sequences of the time series into two states by fitting a Hidden Markov Model (HMM) as explained in Section 3.3. For sub-sequences belonging to a specific state, the suitability of four different models are studied in Section 3.4. The residuals from fitting the different trajectories to these models are analyzed in Section 3.5 and the underlying distribution detected in Section 3.6. The suitability of the proposed models to predict future solar flare emissions using back-testing is studied in Section 3.7.

3.1 Data Preparation

The solar flare event data is collected from the X-ray sensors (XRS) on the GOES [26] satellites provided by the NOAA Space Weather Prediction Center (SWPC). The data consists of X-ray fluxes from two channels: a short channel (wavelength bands of 0.5 to 4 $\mathring{A}$) and a long channel (wavelength 1 to 8 $\mathring{A}$). These XRS channels are prone to saturate under extreme flare events. We use 1-min long channel saturated readings from the GOES-13, GOES-14 and GOES-15 satellites [26] for the time period 01-Jul-2017 to 30-Sep-2017. In order to get the true fluxes, the SWPC scaling factors are removed by dividing the XRS flux from long channel by 0.7 [27]. The two bands of X-rays: 1-8 $\mathring{A}$ band and 0.5-4 $\mathring{A}$ band are also called soft and hard X-ray emission respectively. In this paper, we use the X-ray fluxes from the long channel or soft X-ray emissions. For the month of July and September 2017, data is available from both GOES-13 and GOES-15 satellites. For the month of August 2017, data is available from three satellites: GOES-13, GOES-14 and GOES-15. For those time points for which multiple readings exist, we take the average of the available readings

else we take the maximum of the readings. As a result, the resulting time series for July 2017 is of length 44640, out of which 44416 values are an average of both GOES-13 and GOES-15 readings and the remaining 224 values are the maximum of the reading. Similarly, we have a time series of length 43200 for September 2017 of which 39239 readings from GOES-13 and GOES-15 satellites are averaged. For August 2017, we use reading from GOES-13, GOES-14 and GOES-15 satellites, of which 2852 values are an average of three readings, 2852 values are average of two readings and remaining 1984 is the maximum of available one reading. On 23rd August 2017, none of the three satellites captured X-ray flux readings between 17:03 and 17:11. We remove these readings from our dataset resulting in a time series of length 44631. The time series for the three months are shown in Figures 3.1-3.3.

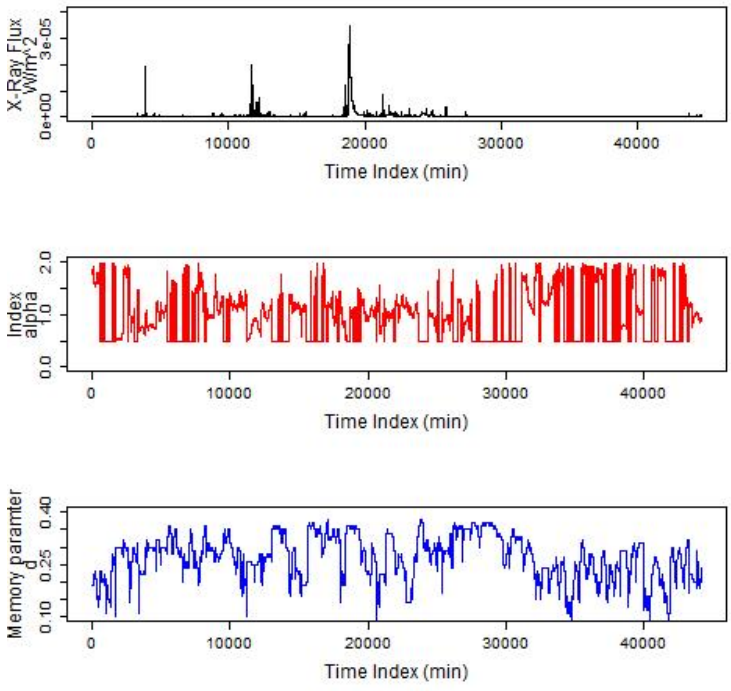

Figure 3.1 Time series plot, α and d estimates of the solar flare energy for July 2017

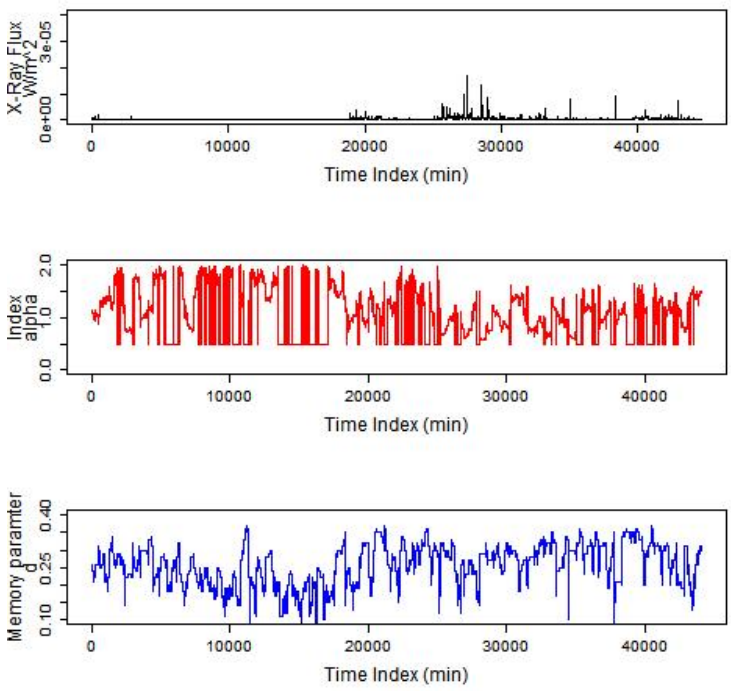

Figure 3.2 Time series plot, α and d estimates of the solar flare energy for August 2017

3.2 Memory and Heavy tail parameter estimation

In this section we study the long range dependence and the heavy tail index of the time series by estimating long memory parameter d and the stability parameter α.

First, we need to identify the dependence in our time series data using visual methods and by estimating the memory parameter, d. We use three methods to estimate d. The first method is the R/S method which was developed by Hurst [28]. The other two estimators are the Geweke and Porter-Hudak (GPH) estimator based on the log-periodogram [29] and a modified semiparametric local whittle estimator [30]. Since the values of the estimates are close to each other, we use the modified semiparametric local whittle estimator [30].

Next, to check if the data follows heavy tails, we estimate the stability parameter α using three methods. The first one is a maximum likelihood method based on the probability distribution [31]. The second method is a quantile based method called McCulloch estimation [32]. The third

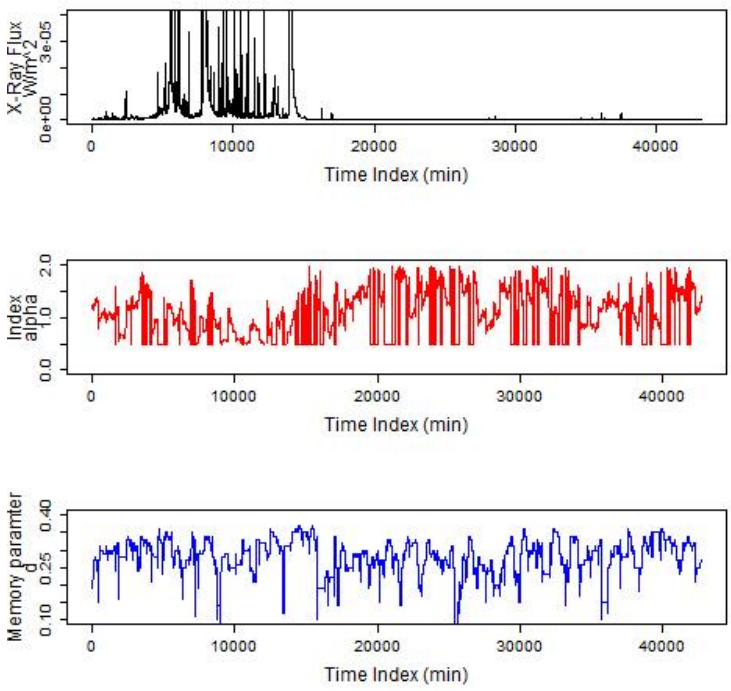

Figure 3.3 Time series plot, α and d estimates of the solar flare energy for September 2017

method is a combination of the Kogon regression method based on the characteristic function and the McCulloch quantile method [33]. The maximum likelihood is very slow and hence we use the last two estimation methods for estimating α. It is suggested in [34] that we try all three methods and pick the mode of the estimates. Since the value of estimates are close to each other, we use the estimate from the Kogon regression method [33]. These methods are available in the `StableEstim` R package.

The values of these parameter estimates vary with time and are observed to be constant if using short samples of length 512 [11]. The α parameter estimate using the McCulloch estimation method and the long memory parameter estimate, d using the R/S method [35] is performed for a rolling window of 512 data points as shown in Figures 3.1-3.3. As illustrated in Figures 3.1-3.3, the high peaks in X-ray fluxes for the three months is associated with lower α values close to 1.0 and higher d values close to or greater than 0.3. The values of α is close to 2, and memory parameter d is close to 0.1-0.2 when the X-ray fluxes don't peak.

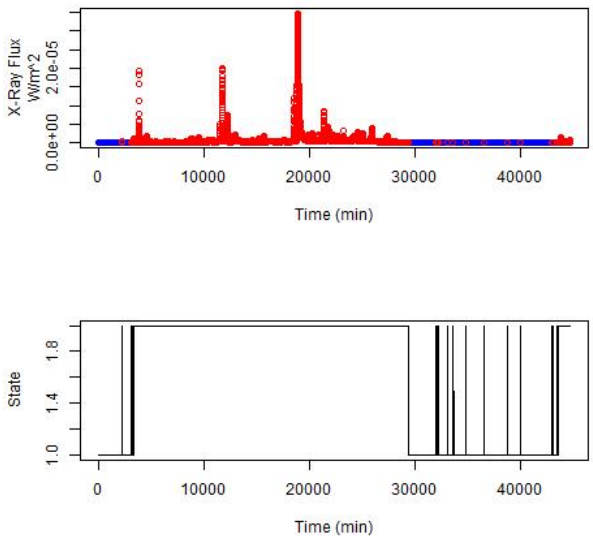

Figure 3.4 Time series plot (top) and States from an HMM fit (bottom) for July 2017 solar flare time series

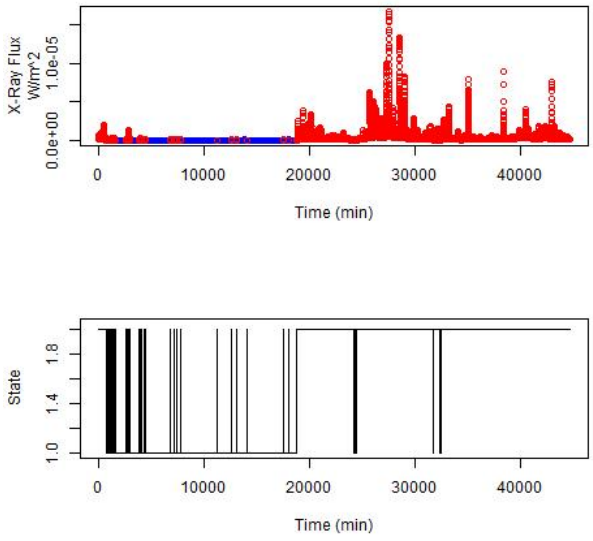

Figure 3.5 Time series plot (top) and States from an HMM fit (bottom) for August 2017 solar flare time series

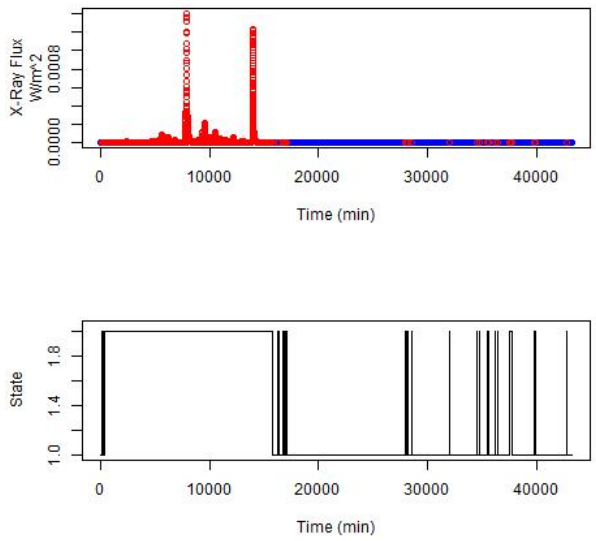

Figure 3.6 Time series plot (top) and States from an HMM fit (bottom) for September 2017 solar flare time series

3.3 Fitting a Hidden Markov Model

Hidden Markov Model (HMM) is a statistical Markov model which assumes that the observation, X_t is generated at time, t by another process with a hidden state, S_t. These hidden states satisfy the Markov property, see [36] for more details. The observed process, X_t can belong to two states depending on the values of S_t. The values of the states are discrete and not observable. The probability of transitioning from state i at time t to state j at time $t+1$ is called a transition probability, $p_{ij} = P(S_{t+1} = j|S_t = i)$. The emission probability, $P(X_t|S_t)$ is the probability of an observation, X_t in a hidden state, S_t. We use these probabilities to compute the joint probability distribution, $f(X, S)$ where X is the observed sequence and S is the vector of hidden states. In order to estimate the parameters of the HMM model, we use the Expectation-Maximization (EM) algorithm [37]. Given $\Theta^{(0)}$, the starting value for parameters of the HMM model, the EM algorithm constitutes the following two steps which is executed for a number of iterations until it converges and finds a local maximum.

1. Expectation Step: Using values from the previous step, compute the expectation of the joint distribution $E[\ln f(X, S; \Theta^{(n)})]$

2. Maximization Step:
   $\Theta^{(n+1)} = \max_{\Theta} E[\ln f(X, S; \Theta^{(n)})]$

In Figures 3.1-3.3 we can see how the α and d paramters are stable for short periods of time before changing again. Since $\alpha \sim 2$ indicates the time series has an underlying Gaussian distribution, we see two states in this plot: one when $\alpha \sim 2$ and one when α is not close to 2. In order to identify these states, we fit the time series to a two state Hidden Markov Model (HMM) with Gaussian distribution. Therefore, the Markov process generates a value X_t based on the two hidden states.

$$X_t = X_{t,1} \text{ if } S_t = 1$$

$$X_t = X_{t,2} \text{ if } S_t = 2$$

$$\text{where } X_{t,i} \sim N(\mu_i, \sigma_i^2) \text{ and } i\text{=}1,2$$

The distribution of these values follow a Gaussian distribution which makes it easier to compute the joint probability. We use the `depmixs4` R package [38] to fit the HMM model to the log transformed data-set. To make sure the states are consistent, the data for three months must be fit as a single time series which is of length 132,471.

Figures 3.4-3.6 shows the states extracted from time series between July and August 2017 fitted by the 2-state HMM model. Comparing Figures 3.1-3.3 and Figures 3.4-3.6, we see that State 1 indicates $\alpha \sim 2$ and lower d, and State 2 indicates a lower $\alpha < 2$ and higher d. Also, the peaks are more pronounced in State 2 than State 1.

3.4 Modeling the solar-flare time series

In this section, we fit a shorter sample of length 500-2000 belonging to State 1 and State 2 for the time series from the three months using 4 different time series models: ARTFIMA, ARFIMA, ARTFIMA-GARCH, and ARFIMA-GARCH. The time series samples chosen for each month is

Table 3.1 Time indexes of selected trajectories of State 1 and State 2 data along with estimates of α and d

	Month	Time Index Range	α	d
State 1	Jul	1:1000	1.957	0.343
	Aug	15000:17000	1.999	0.267
	Sep	23500:25500	1.630	0.656
State 2	Jul	7400:8400	1.639	0.722
	Aug	35000:36000	1.197	0.999
	Sep	10000:11000	0.994	0.848

shown in Table 3.1. The time series plots for the selected trajectories for State 1 are shown in Figure 3.7-3.9, and the time series plots for the selected trajectories for State 2 are shown in Figure 3.10-3.12

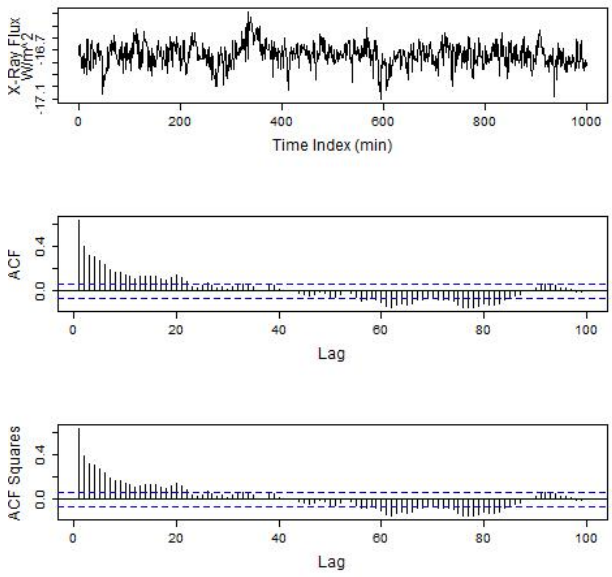

Figure 3.7 Times series (top), ACF of time series (middle) and ACF of squared time series (bottom) of log transformed data for State 1 trajectory of July 2017 data

First, we need to make sure the data is stationary. In order to do that, we take the log-transform of the data and use a shorter length time series as shown in Table 3.1. The Augmented Dickey-Fuller test [39] rejects the null hypothesis for lack of unit-root stationarity with a p-value of 0.01 for all the trajectories in Table 3.1. The State 1 and State 2 trajectories for July 2017

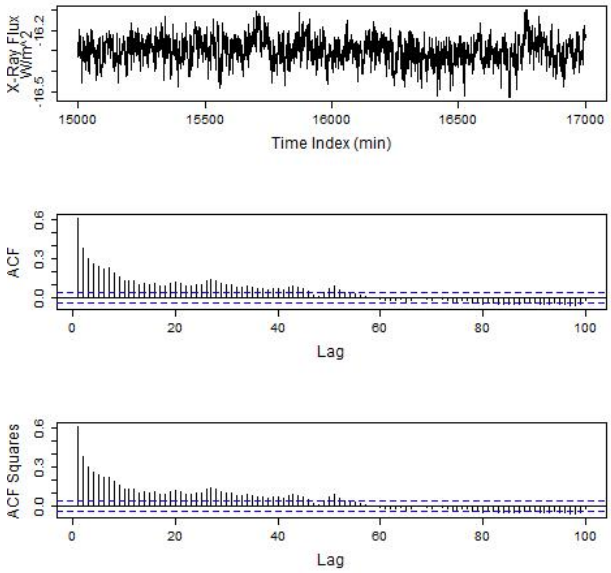

Figure 3.8 Times series (top), ACF of time series (middle) and ACF of squared time series (bottom) of log transformed data for State 1 trajectory of August 2017 data

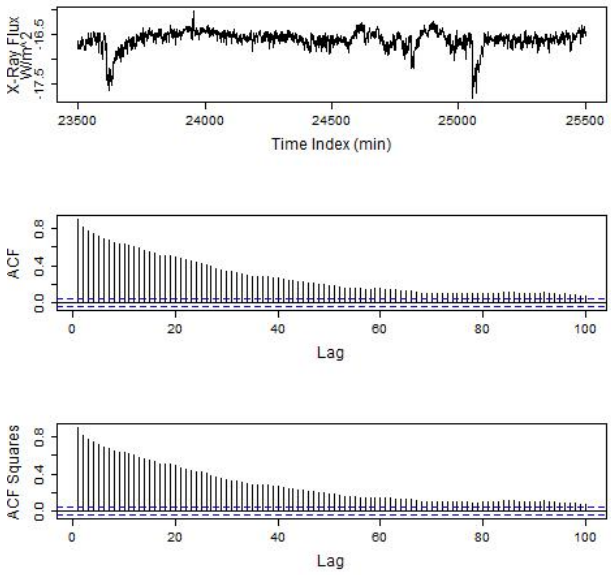

Figure 3.9 Times series (top), ACF of time series (middle) and ACF of squared time series (bottom) of log transformed data for State 1 trajectory of September 2017 data

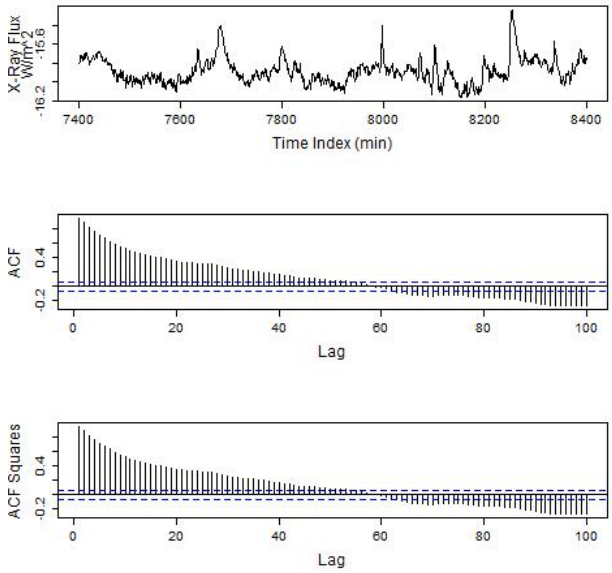

Figure 3.10 Times series (top), ACF of time series (middle) and ACF of squared time series (bottom) of log transformed data for State 2 trajectory of July 2017 data

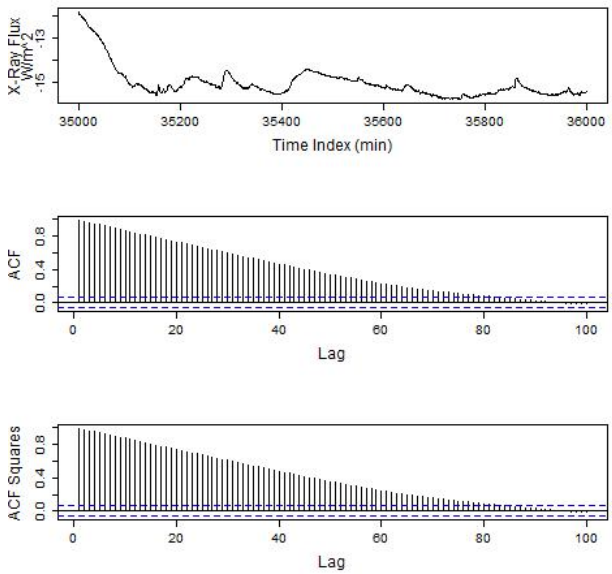

Figure 3.11 Times series (top), ACF of time series (middle) and ACF of squared time series (bottom) of log transformed data for State 2 trajectory of August 2017 data

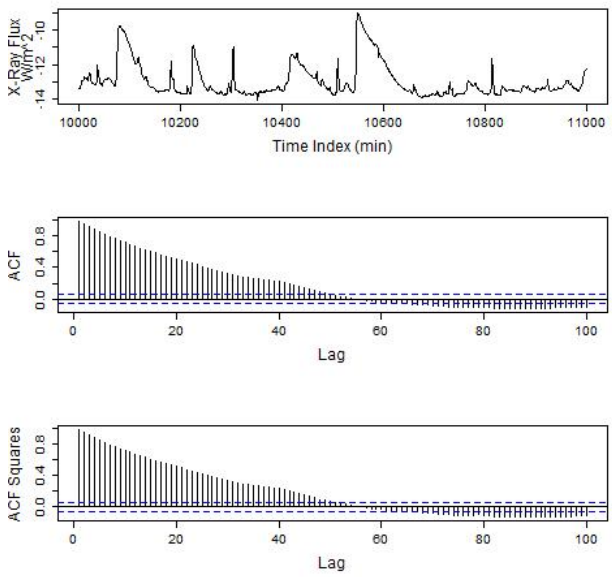

Figure 3.12 Times series (top), ACF of time series (middle) and ACF of squared time series (bottom) of log transformed data for State 2 trajectory of September 2017 data

fails to reject null hypothesis of trend stationarity using the KPSS test [40]. The ACF plots of the sample trajectories are shown in Figure 3.7-3.9 and Figures 3.10-3.12 for the months July, August and September respectively for State 1 and State 2. The ACF plots for the log transformed data and the squared log transformed data indicate evidence of long memory. The stability paramter α estimated using the Kogon regression method [33], and the long memory parameter d estimate using the Hou-Perron method are shown in Table 3.2. The α estimate of State 1 trajectory from July and August 2017 show clear evidence of a Gaussian distribution since $\alpha \sim 2$. The long memory parameter estimates $d > 0.5$ for all the State 2 trajectories, which indicates lack of stationarity [41] when using a ARFIMA model.

We fit the log transformed samples of time series with the four models and estimate the parameters of the ARTFIMA and ARFIMA models along with the Akaike Information Criteria (AIC) for all four models as shown in Table 3.2. For the State 1 time series, we fit ARTFIMA$(0, d, \lambda, 1)$, ARTFIMA$(0, d, \lambda, 1)$-GARCH$(1, 1)$, ARFIMA$(0, d, 1)$, and ARFIMA$(0, d, 1)$-GARCH$(1, 1)$ models. For State 2 time series, we fit ARTFIMA$(1, d, \lambda, 1)$, ARTFIMA$(1, d, \lambda, 1)$-GARCH$(1, 1)$, ARFIMA

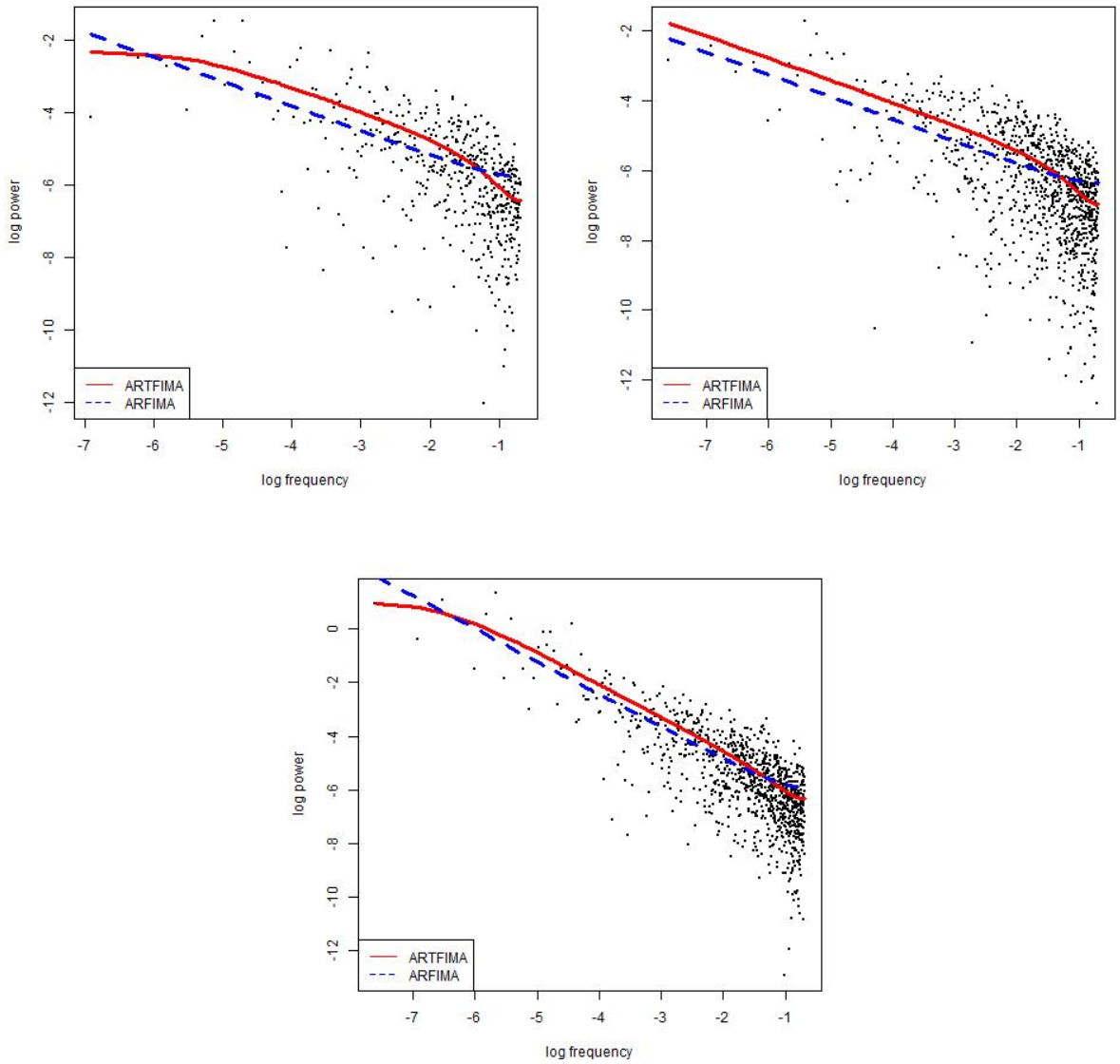

Figure 3.13 Spectral density of State 1 data for July with $d = 0.334, \lambda = 0.027$(top-left), August with $d = 0.321, \lambda = 0.0009$ (top-right) and September with $d = 0.609, \lambda = 0.009$ (bottom) 2017 trajectories along with the fitted ARTFIMA and ARFIMA spectrum

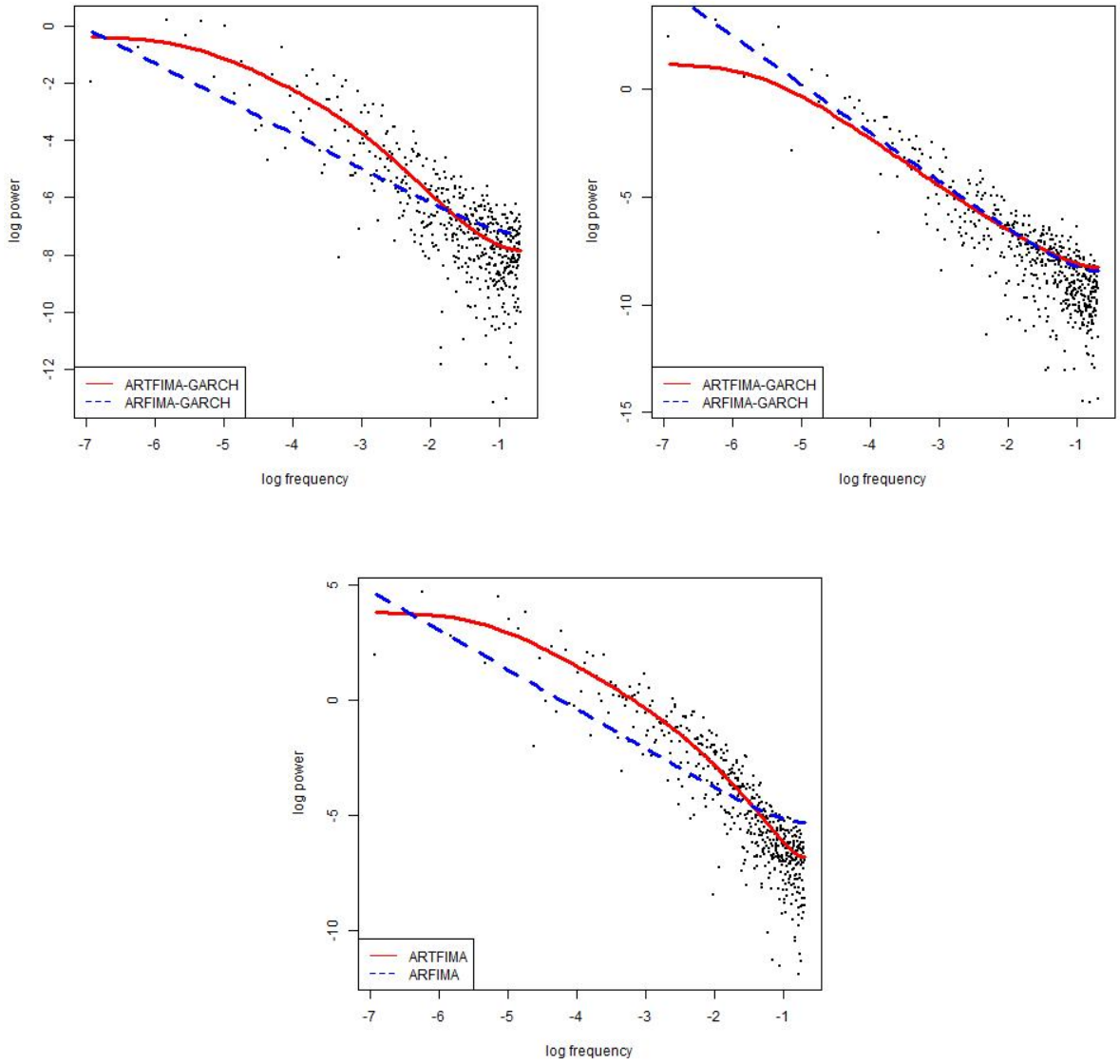

Figure 3.14 Spectral density of State 2 data for July with $d = 0.611, \lambda = 0.026$ (top-left), August with $d = 1.122, \lambda = 0.024$ (top-right) 2017 data along with the fitted ARTFIMA-GARCH and ARFIMA-GARCH spectrum. Spectral density of State 2 data for September with $d = 0.858, \lambda = 0.029$ (bottom) 2017 data along with the fitted ARTFIMA and ARFIMA spectrum

Table 3.2 AIC and parameter estimates for four different models on four trajectories of solar-flare data

	Month	d	ARTFIMA						ARTFIMA-GARCH	ARFIMA					ARFIMA-GARCH
			(p,q)	*AIC*	Φ	Θ	d	λ	*AIC*	(p,q)	*AIC*	Φ	Θ	d	*AIC*
State1	Jul	0.343	(0,1)	-2431.34	NA	(-0.292)	0.339	0.027	-2441.286	(0,1)	-2430.34	NA	(-0.309)	0.312	-2438.576
	Aug	0.267	(0,1)	-6162.09	NA	(-0.263)	0.321	0.00088	-6162.088	(0,1)	-6162.93	NA	(-0.277)	0.301	-6172.134
	Sep	0.656	(0,1)	-4445.38	NA	(-0.197)	0.609	0.009	-4670.93	(0,1)	-4416.99	NA	(-0.304)	0.489	-4668.058
State2	Jul	0.722	(1,1)	-3474.82	(0.652)	(0.225)	0.611	0.026	-3630.38	(1,1)	-3297.8	(0.241)	(-0.036)	0.489	-3537.45
	Aug	0.999	(1,1)	-3847.54	(0.213)	(0.306)	1.122	0.024	-4327.822	(1,1)	-2189.76	(0.253)	(-0.014)	0.490	-3368.488
	Sep	0.848	(1,1)	-1239.26	(0.502)	(-0.304)	0.858	0.029	-3234.306	(1,1)	-1225.88	(0.784)	(-0.361)	0.489	-3251.13

$(1, d, 1)$, and ARFIMA$(1, d, 1)$-GARCH$(1, 1)$ models. The order chosen is the order that minimizes the AIC. The residuals of ARTFIMA$(0, d, \lambda, 1)$ and ARFIMA$(0, d, 1)$ models are fit with a GARCH model of order $(1, 1)$ under a conditional normal distribution for State 1 resulting in an ARTFIMA$(0, d, \lambda, 1)$-GARCH$(1, 1)$ and ARFIMA$(0, d, 1)$-GARCH$(1, 1)$ model for State 1 trajectories. The residuals of ARTFIMA$(1, d, \lambda, 1)$ and ARFIMA$(1, d, 1)$ models are fit with a GARCH model of order $(1, 1)$ under a conditional standardized student-t distribution for State 2 resulting in an ARTFIMA$(1, d, \lambda, 1)$-GARCH$(1, 1)$ and ARFIMA$(1, d, 1)$-GARCH$(1, 1)$ model for State 2 trajectories.

We use the `artfima` R package to fit the ARTFIMA and ARFIMA models. We use the `fGarch` R package to fit the residuals using the GARCH model. The Akaike Information Criteria (AIC) for ARTFIMA and ARFIMA are obtained from the artfima function. We calculate the AIC for the GARCH model using the formula -2*logLikelihood+2k where k is the number of parameters. For State 1, we use maximum likelihood estimation to estimate the parameters of both ARTFIMA and ARFIMA models since $\alpha \sim 2$. For State 2, we use whittle estimation for estimating parameters of both ARTFIMA and ARFIMA models since α is not close to 2.

From Table 3.2, for the August 2017 State1 data and Sepember 2017 State 2 trajectory, ARFIMA-GARCH minimizes the AIC. In all other time series, ARTFIMA-GARCH minimizes the AIC for both State 1 and State 2 time series. For State 1, ARTFIMA has an AIC close to ARTFIMA-GARCH and an AIC lower that ARFIMA and ARFIMA-GARCH.

For both the State 1 and State 2 trajectories the tempering paramter, λ estimates in non-zero. The estimates of long memory parameter, d from the ARTFIMA model is close to the one estimated by Hou-Perron method [30]. For the State 1 September 2017 trajectory when $d > 0.5$, fitting the

data with ARFIMA$(0, d, 1)$ leads to a non-stationary model. The same reasoning is true for all State 2 trajectories with $d > 0.5$. In these cases, the ARFIMA model is misspecified and it is appropriate to use the ARTFIMA or ARTFIMA-GARCH model. In the other cases, using the AIC value we do not see much gain in adding extra parameters by choosing an ARTFIMA over an ARFIMA model. Hence, we need to take a closer look at the spectral density of the data.

The log-log plot of the spectral density of ARTFIMA and ARFIMA models along with that of the data is shown in Figures 3.13 and 3.14.

For the State 1 trajectories, the values of the tempering paramter, λ is very less compared to State 1 trajectories, which indicates a small deviation between the fitted lines of ARTFIMA and ARFIMA spectral density as seen in Figure 3.13. Eventhough the value of λ is small, the ARFIMA model does not seem to fit the data for lower and moderate frequencies unlike the ARTFIMA model. The effect of tempering is apparent, particularly for July and September 2017 State 1 trajectory. This is because the spectral density from ARTFIMA model levels off at lower frequencies and fits the periodograms from the data better. The spectral density from ARFIMA model diverges from the periodogram of the actual data at the lower and higher frequencies. Hence, we choose ARTFIMA$(0, d, \lambda, 1)$ as our preferred model for State 1 trajectories.

In Figure 3.14, it is apparent that the spectral density ARTFIMA model fits the periodogram for State 2 trajectories. This is due to the effect of tempering parameter which is larger for the fitted ARTFIMA model on State 2 trajectories. For State 2, ARTFIMA$(1, d, \lambda, 1)$-GARCH$(1, 1)$ has an AIC that is significantly lower than all the other three models. The long memory parameter, d estimated by whittle estimation for ARTFIMA model is close to the estimate by Hou-Perron method [30]. When $d > 0.5$, the ARFIMA model is misspecified. From Table 3.2, it is evident that the ARTFIMA$(1, d, \lambda, 1)$-GARCH$(1, 1)$ model minimizes the AIC as well. Hence, we choose ARTFIMA$(1, d, \lambda, 1)$-GARCH$(1, 1)$ as our preferred model for State 2 trajectories. But, for September 2017 State 2 trajectory, the parameter estimates from the ARTFIMA-GARCH models does not satisfy the condition $\alpha_1 + \beta_1 < 1$ indicating a non-stationary model. Hence, we use an ARTFIMA$(1, d, \lambda, 1)$ for State 2 September 2017 trajectory.

3.5 Residual Analysis

In this section, we analyze the residuals and the squared residuals from the models fitted to the six time series trajectories from Section 3.4. We use the Ljung-Box test [42] to analyze the independence of residuals and the Mc-Leolid Li test [43] for testing the independence of the square residuals. We use the Lagrange multiplier test for lack of ARCH effects [44]. Along with these statistics, we also rely on visual analysis of the residual and ACF of residuals and squared residuals from the model fits as shown in Figures 3.15-3.17 and Figure 3.18-3.20 for the months July, August and September for State 1 and State 2 respectively.

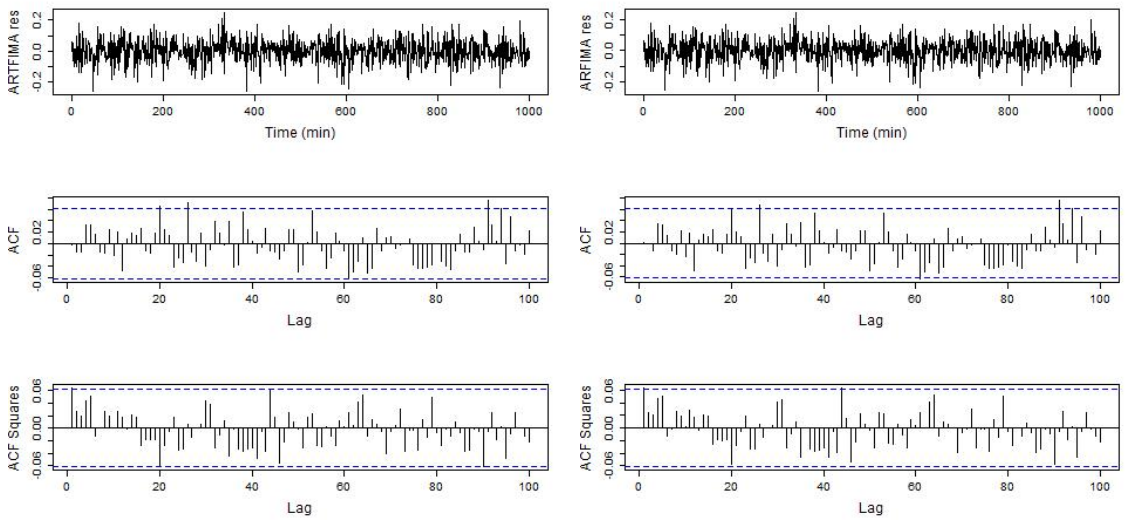

Figure 3.15 Comparison of residuals and ACF plots of residuals and squared residuals between the ARTFIMA (left) and ARFIMA (right) model fitted with the log transformed data for State 1 trajectory of July 2017 data

The Ljung–Box test [42] is a statistical test to check whether the sample autocorrelation is different from zero. It is based on the Ljung-Box statistic, a large value of the statistic indicates that the sample auto correlation is too large for an i.i.d sequence. The Mc-Leolid Li test [43] checks conditional heteroskedascity by performing the Ljung–Box test with the squared data. Both Ljung–Box and Mc-Leolid Li tests compute a p-value that determines whether or not to reject the null hypothesis of i.i.d sequence of data. In this section, the data tested for randomness is

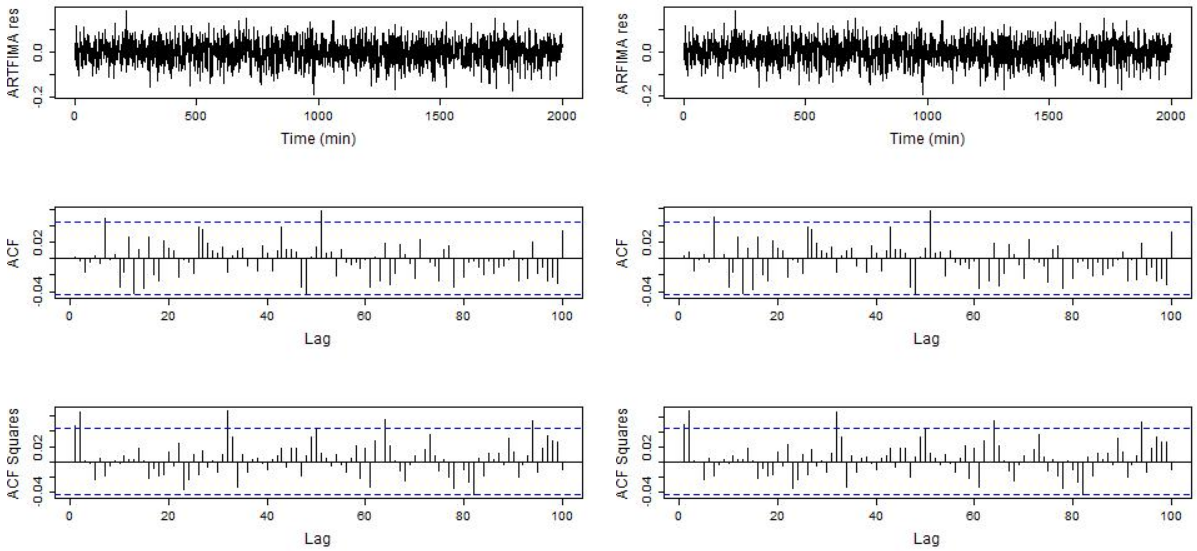

Figure 3.16 Comparison of residuals and ACF plots of residuals and squared residuals between the ARTFIMA (left) and ARFIMA (right) model fitted with the log transformed data for State 1 trajectory of August 2017 data

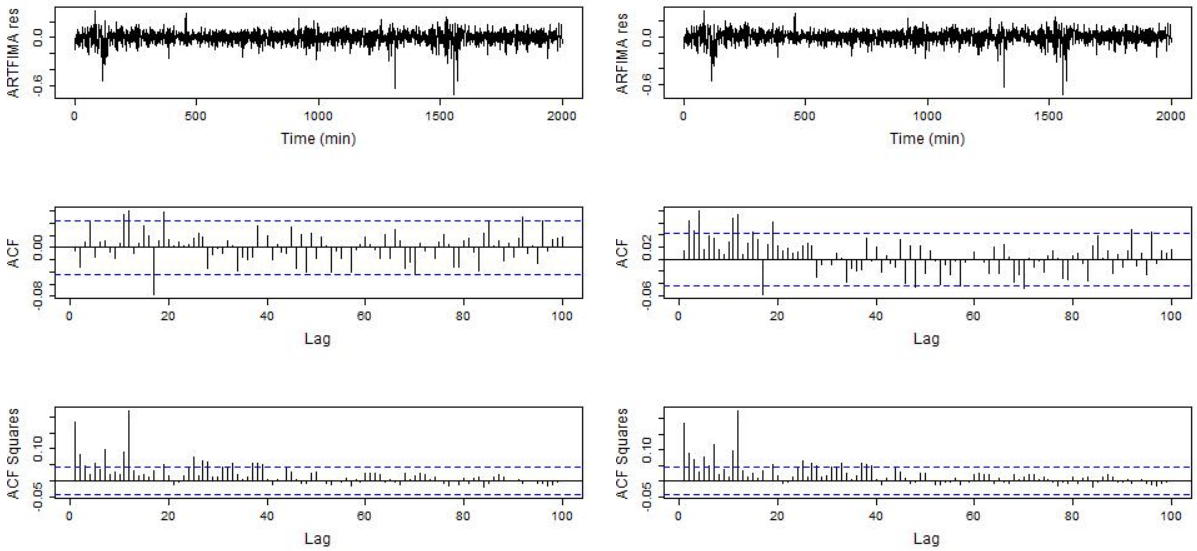

Figure 3.17 Comparison of residuals and ACF plots of residuals and squared residuals between the ARTFIMA (left) and ARFIMA (right) model fitted with the log transformed data for State 1 trajectory of September 2017 data

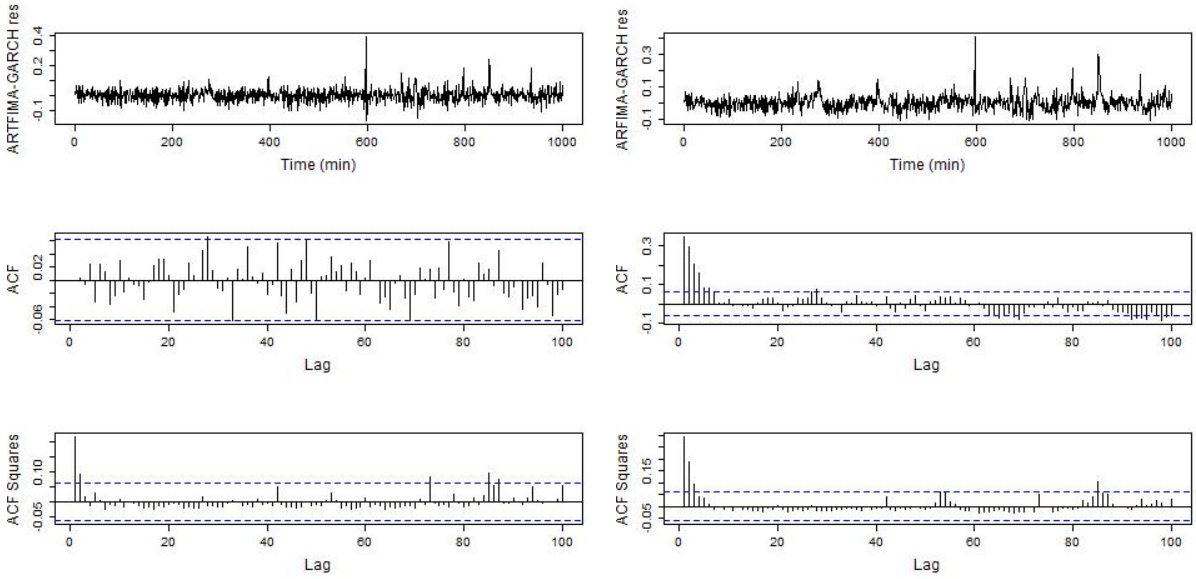

Figure 3.18 Comparison of residuals and ACF plots of residuals and squared residuals between the ARTFIMA-GARCH (left) and ARFIMA-GARCH (right) model fitted with the log transformed data for State 2 trajectory of July 2017 data

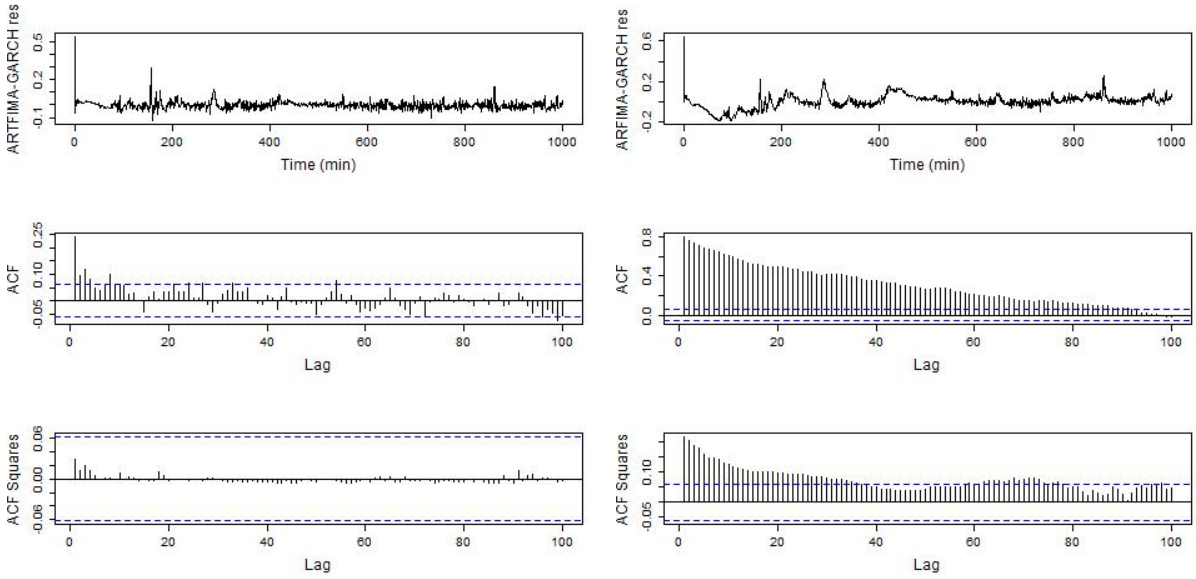

Figure 3.19 Comparison of residuals and ACF plots of residuals and squared residuals between the ARTFIMA-GARCH (left) and ARFIMA-GARCH (right) model fitted with the log transformed data for State 2 trajectory of August 2017 data

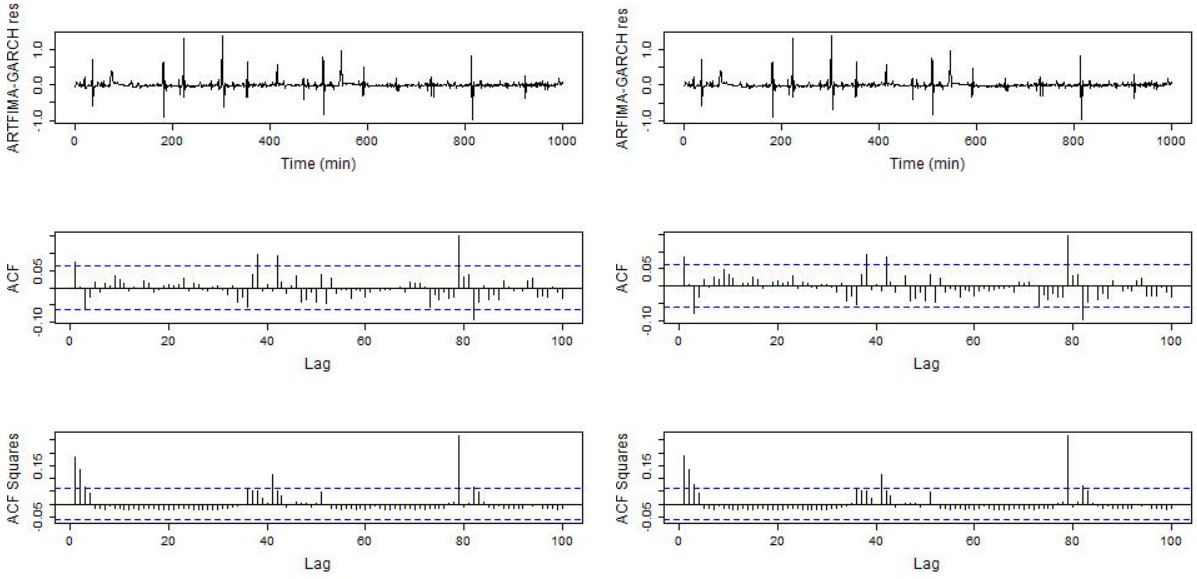

Figure 3.20 Comparison of residuals and ACF plots of residuals and squared residuals between the ARTFIMA-GARCH (left) and ARFIMA-GARCH (right) model fitted with the log transformed data for State 2 trajectory of September 2017 data

the residuals from an ARTFIMA or ARTFIMA-GARCH model. However, the residuals from a GARCH model must be tested for GARCH effects. For this we use a Lagrange Multiplier (LM) test [44] that has a null hypothesis of no GARCH disturbances by testing if the coefficients of the GARCH model $a_0 = a_1 = ... = a_k = 0$ and $b_0 = b_1 = ... = b_l = 0$.

For both July and August 2017 State 1 trajectory, we can verify the independence of residuals and square residuals for both ARTFIMA and ARFIMA models. We observe from the ACF plots in Figures 3.15 and 3.16 that for both the residuals and the squared residuals the ACF is within the 95% confidence interval. For the State 1 trajectories, the ACF plots don't show much difference in case of ARTFIMA and ARFIMA. Hence, we need to rely on statistical tests. For State 1 July 2017 data, the p-value from the Ljung box and McLeoli-Li test for ARTFIMA and ARFIMA model residuals is (0.857, 0.559) and (0.886, 0.566) at lag 20 respectively. We see a similar result for August 2017 State 1 trajectory, with p-values from the Ljung box and McLeoli-Li test for ARTFIMA and ARFIMA is (0.381, 0.552) and (0.377, 0.505) at lag 20 respectively. For September 2017 State

1 trajectory, the p-values from the Ljung box and McLeoli-Li test for ARTFIMA and ARFIMA are (0.65, < 0.001) and (< 0.001, < 0.001) at lag 15 respectively, which indicates that ARTFIMA residuals are independent whereas ARFIMA shows lack of independence of both residuals and squared residuals. Hence, we can conclude from the residual analysis for State 1 trajectories, that ARTFIMA model residuals and squared residuals show evidence of independence through both ACF plots and statistical tests except for September 2017 for which the ARTFIMA model residuals satisfy independence of residuals but not squared residuals.

For July 2017 State 2 trajectory, we can verify the independence of residuals and square residuals for the ARTFIMA-GARCH case. The ARFIMA-GARCH residuals lack independence but the square residuals show evidence of independence as the ACF is within the 95% confidence interval. The p-value from the Ljung box, McLeoli-Li and LM test for ARTFIMA-GARCH and ARFIMA-GARCH are (0.965, 0.995, 0.886) and (< 0.001, 0.998, 0.974) at lag 20 respectively. Both residuals and squared residuals from ARTFIMA-GARCH show evidence independence, where-as residuals from ARFIMA-GARCH show lack of independence. The lack of fit of residuals in the ARFIMA-GARCH model is also obvious from Figure 3.18, since the ACF of the residuals lie outside the 95% confidence interval. For the August 2017 State 2 trajectory, we have p-values from the Ljung box, McLeoli-Li, and LM test for ARTFIMA-GARCH and ARFIMA-GARCH are (< 0.001, 0.99, 0.97) and (< 0.001, 0.99, 0.594) at lag 20 respectively. In this case, the residuals from both models lack independence whereas the squared residuals show evidence of independence and the residuals fail to reject null hypothesis for GARCH effects. The lack of fit of residuals in the ARFIMA-GARCH model is also obvious from Figure 3.19, since the ACF of the residuals lie outside the 95% confidence interval. For the September 2017 State 2 trajectory, the ACF plots in Figure 3.20 don't show much difference in case of ARTFIMA and ARFIMA. The p-values of the Ljung box, McLeoli-Li, and LM test for ARTFIMA-GARCH and ARFIMA-GARCH are (0.285, 0.999, 0.999) and (0.015, 0.999, 0.999) at lag 20 respectively. The squared residuals from both models are independent and lack GARCH effects. But the residuals from the ARFIMA-GARCH modes lacks independence.

By examining the independence of residuals and square residuals for State 1 trajectories, the ARTFIMA model performs better than the ARFIMA model. Similarly, by comparing the independence of residuals and square residuals for State 2 trajectories and testing for evidence of GARCH effects, we observe that ARTFIMA-GARCH model is preferred over the ARFIMA-GARCH model.

3.6 Distribution of Residuals

In this section, we identify the distribution of the ARTFIMA residuals for the State 1 trajectories and the distribution of ARTFIMA-GARCH residuals for the State 2 trajectories. We use the Kolmogorov-Smirnov statistic [45] to detect the underlying distribution of residuals using empirical cumulative distriction function, $F_N(x)$ and the theroritical cumulative distribution function, $F(x)$. The Kolmogorov-Smirnov statistic, $D = \sup_x\{|F_N(x) - F(x)|\}$. The p-value is computed under the null hypothesis that the empirical distribution is same as the theoretical distribution. We compute the p-value based on 1000 monte-carlo simulations of the samples from the suspected underlying distribution. We compute the statistic from the original data and from the Monte-Carlo simulation, and compute the p-value as the proportion of the statistical value that is close to the one from the original data. If the p-value is < 0.05, we reject the null hypothesis.

The suspected underlying distributions that we test the original data are the Gaussian, Stable, Fractional Gaussian, and Tempered α-stable distribution. The p-values are 0.44, 0.34, and 0.05 respectively using the Kolmogorov-Smirnov statistic for the July, August, and September 2017, State 1 trajectory against a Gaussian distribution N(δ,$2\gamma^2$) derived using the McCulloch stable distribution parameter estimation method [34] that estimates the parameters of a stable distribution $S(\alpha, \beta, \gamma, \delta)$. The State 2 trajectories does not follow a Gaussian distribution but a stable distribution with a p-value of 0.15, 0.423, and 0.324 respectively. Since we fit our distributions with an ARTFIMA distribution, the tempering effect has been removed in the residuals and none of the residuals fit the tempered α-stable distribution.

3.7 Model Back-testing

In this section, we do a one-step prediction from a sample of State 1 time series using the ARTFIMA model and another one-step prediction from a sample of State 2 time series using the ARTFIMA-GARCH model. We calculate the distribution of the prediction width using a 95% bootstrap prediction interval over 1000 iterations.

For the ARTFIMA models, we use a k-step linear predictor based on the historical data defined as

$$\hat{X}_{n+k} = \sum_{j=0}^{n} a_j X_{n-j}$$

The model proposed for the trajectories in Table 3.1 based on our study in previous sections is as follows.

July 2017 State 1:

$$(1 - e^{-0.027}B)^{0.339} X_t = Z_t - 0.292 Z_{t-1}$$

Z_t follows a i.i.d normal distribution

August 2017 State 1:

$$(1 - e^{-0.0009}B)^{0.321} X_t = Z_t - 0.263 Z_{t-1}$$

Z_t follows a i.i.d normal distribution

September 2017 State 1:

$$(1 - e^{-0.009}B)^{0.609} X_t = Z_t - 0.197 Z_{t-1}$$

Z_t follows a i.i.d normal distribution

July 2017 State 2:

$$(1 - e^{-0.026}B)^{0.611} X_t - 0.652 X_{t-1} = Z_t + 0.225 Z_{t-1}$$

$$Z_t = \sqrt{h_t}\mu_t$$

$$h_t = 9.471 \times 10^{-4} + 0.138 Z_{t-1} + 0.286 h_{t-1}$$

μ_t follows a standardized student-t distribution with 7 degrees of freedom

August 2017 State 2:

$$(1 - e^{-0.024}B)^{1.122} X_t - 0.212 X_{t-1} = Z_t + 0.306 Z_{t-1}$$

$$Z_t = \sqrt{h_t}\mu_t$$

$$h_t = 1.441 \times 10^{-4} + 0.262 Z_{t-1} + 0.598 h_{t-1}$$

μ_t follows a standardized student-t distribution with 6 degrees of freedom

September 2017 State 2:

$$(1 - e^{-0.029}B)^{0.858} X_t - 0.502 X_{t-1} = Z_t - 0.304 Z_{t-1}$$

Z_t follows a i.i.d stable distribution.

We analyze the predictions for two trajectories from July and August 2017 belonging to State 1 and State 2 respectively. The predictions for 500 time steps using the one step ARTFIMA model prediction on July 2017 State 1 trajectory is shown in Figure 3.21. The plot also shows the prediction interval which has a very narrow median prediction width of 0.25. The predictions for 400 time steps using the one step ARTFIMA-GARCH model prediction on August 2017 State 2 trajectory is shown in Figure 3.22. The prediction interval shows that the predictions and the actual values lie within a very narrow median prediction width of 0.15. The log values can be transformed back to the original form using the exponential operator.

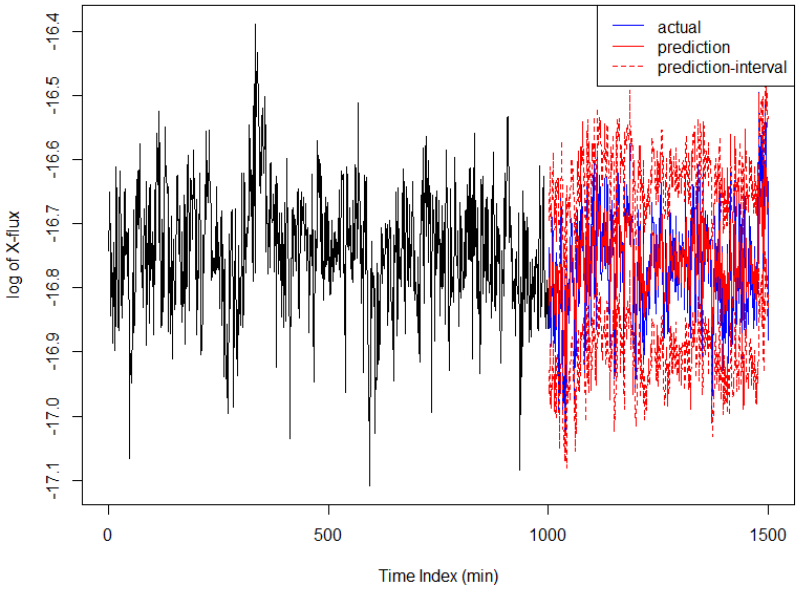

Figure 3.21 One step predictions and prediction interval for 500 time points of State 1 time series trajectory for July 2017 using ARTFIMA model

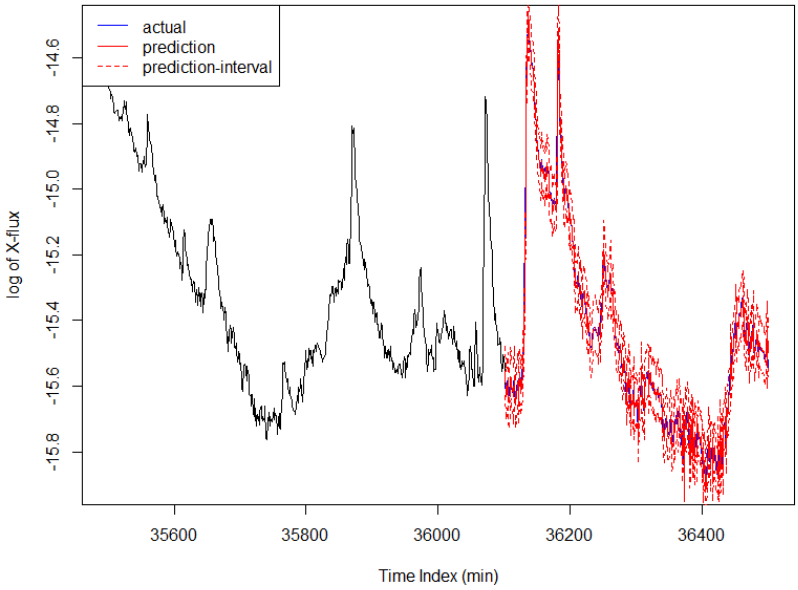

Figure 3.22 One step predictions and prediction interval for 400 time points of State 2 time series trajectory for August 2017 using ARTFIMA-GARCH model

CHAPTER 4. SUMMARY & DISCUSSION

In this work, we use a time series model ARTFIMA and ARTFIMA-GARCH to fit the solar soft X-ray emission during a period of solar minimum. We also demonstrate the parameter estimation of stable ARTFIMA time series using the whittle estimation method. We compare the results of ARTFIMA and ARTFIMA-GARCH models to that of ARFIMA and ARFIMA-GARCH models as studied in [11]. Using both visual and statistical analysis, the State 1 trajectories fit the ARTFIMA(0,d,λ,1) model better than the ARFIMA model, and the ARTFIMA(1,d,λ,1)-GARCH(1,1) model fits better than the ARFIMA-GARCH model for the State 2 trajectories. We show that the residuals from these models fit a normal distribution in case of State 1 trajectories and a stable distribution in case of State 2 trajectories using statistical tests. We also predict the future solar X-ray for the next one minute using the ARTFIMA for a sample State 1 trajectory and ARTFIMA-GARCH model for a sample State 2 trajectory. We observe a very narrow prediction width using a 95% bootstrap prediction interval for the trajectories studies which shows the usefulness of the ARTFIMA and ARTIMA-GARCH models to predict solar flare emissions. For future work, we plan to fit the data for the period of solar maximum with the ARTFIMA model and compare it with the ARFIMA model which was studied in [8].

BIBLIOGRAPHY

[1] Meerschaert, M. M., F. Sabzikar, M. S. Phanikumar, and A. Zeleke (2014). Tempered fractional time series model for turbulence in geophysical flows. *Journal of Statistical Mechanics: Theory and Experiment 2014*(9), P09023.

[2] Sabzikar, F., I. McLeod, and M. M. Meerschaert (2018). Parameter estimation for artfima time series. *Journal of Statistical Planning and Inference*.

[3] Stuck, B. W. and B. Kleiner (1974). A statistical analysis of telephone noise. *Bell System Technical Journal 53*(7), 1263–1320.

[4] Fama, E. F. (1965). The behavior of stock-market prices. *The journal of Business 38*(1), 34–105.

[5] Stuck, B. (1978). Minimum error dispersion linear filtering of scalar symmetric stable processes. *IEEE Transactions on Automatic Control 23*(3), 507–509.

[6] Burnecki, K. (2012). Farima processes with application to biophysical data. *Journal of Statistical Mechanics: Theory and Experiment 2012*(05), P05015.

[7] Burnecki, K. and G. Sikora (2017). Identification and validation of stable arfima processes with application to umts data. *Chaos, Solitons & Fractals 102*, 456–466.

[8] Stanislavsky, A., K. Burnecki, M. Magdziarz, A. Weron, and K. Weron (2009). Farima modeling of solar flare activity from empirical time series of soft x-ray solar emission. *The Astrophysical Journal 693*(2), 1877.

[9] NASA. Geostationary operational environmental satellites.

[10] NOAA. National oceanic and atmospheric administration.

[11] Stanislavsky, A. A., K. Burnecki, J. Janczura, K. Niczyj, and A. Weron (2019). Solar x-ray variability in terms of a fractional heteroskedastic time series model. *Monthly Notices of the Royal Astronomical Society 485*(3), 3970–3980.

[12] Sabzikar, F. (2014). *Tempered fractional Brownian motion.*

[13] Sabzikar, F., M. M. Meerschaert, and J. Chen (2015). Tempered fractional calculus. *Journal of Computational Physics 293*, 14–28.

[14] Sabzikar, F. and D. Surgailis (2018). Invariance principles for tempered fractionally integrated processes. *Stochastic Processes and their Applications 128*(10), 3419–3438.

[15] Astrauskas, A., J. Levy, and M. Taqqu (1991). The asymptotic dependence structure of the linear fractional lévy motion. *Lithuanian Mathematical Journal 31*(1), 1–19.

[16] Samorodnitsky, G., M. S. Taqqu, and R. Linde (1996). Stable non-gaussian random processes: stochastic models with infinite variance. *Bulletin of the London Mathematical Society 28*(134), 554–555.

[17] Samoradnitsky, G. (2017). *Stable non-Gaussian random processes: stochastic models with infinite variance*. Routledge.

[18] Kokoszka, P. S. and M. S. Taqqu (1995). Fractional arima with stable innovations. *Stochastic processes and their applications 60*(1), 19–47.

[19] Klüppelberg, C. and T. Mikosch (1994). Some limit theory for the self-normalised periodogram of stable processes. *Scandinavian Journal of Statistics*, 485–491.

[20] Mikosch, T., T. Gadrich, C. Kluppelberg, and R. J. Adler (1995). Parameter estimation for arma models with infinite variance innovations. *The Annals of Statistics*, 305–326.

[21] Beran, J., Y. Feng, S. Ghosh, and R. Kulik (2016). *Long-Memory Processes.* Springer.

[22] Ling, S. and W. K. Li (1997). On fractionally integrated autoregressive moving-average time series models with conditional heteroscedasticity. *Journal of the American Statistical Association 92*(439), 1184–1194.

[23] Almeida, R., C. Dias, M. E. Silva, and A. P. Rocha (2017). Arfima-garch modeling of hrv: clinical application in acute brain injury. In *Complexity and Nonlinearity in Cardiovascular Signals*, pp. 451–468. Springer.

[24] Hosking, J. (1981). Fractional differencing. biometrika 68 165–176. *Mathematical Reviews (MathSciNet): MR614953 Zentralblatt MATH 464*.

[25] Bollerslev, T. (1986). Generalized autoregressive conditional heteroskedasticity. *Journal of econometrics 31*(3), 307–327.

[26] NOAA. Goes x-ray sensor (xrs) measurements.

[27] NOAA. Goes x-ray sensor (xrs) measurements readme.

[28] Hurst, H. E. (1951). Long-term storage capacity of reservoirs. *Trans. Amer. Soc. Civil Eng. 116*, 770–799.

[29] Geweke, J. and S. Porter-Hudak (1983). The estimation and application of long memory time series models. *Journal of time series analysis 4*(4), 221–238.

[30] Hou, J. and P. Perron (2014). Modified local whittle estimator for long memory processes in the presence of low frequency (and other) contaminations. *Journal of Econometrics 182*(2), 309–328.

[31] Nolan, J. P. (2001). Maximum likelihood estimation and diagnostics for stable distributions. In *Lévy processes*, pp. 379–400. Springer.

[32] McCulloch, J. H. (1986). Simple consistent estimators of stable distribution parameters. *Communications in Statistics-Simulation and Computation 15*(4), 1109–1136.

[33] Kogon, S. M. and D. B. Williams (1998). Characteristic function based estimation of stable distribution parameters. *A practical guide to heavy tails: statistical techniques and applications*, 311–338.

[34] Nolan, J. P. (1999). Fitting data and assessing goodness-of-fit with stable distributions. *Applications of Heavy Tailed Distributions in Economics, Engineering and Statistics, Washington DC*.

[35] Weron, R. (2002). Estimating long-range dependence: finite sample properties and confidence intervals. *Physica A: Statistical Mechanics and its Applications 312*(1-2), 285–299.

[36] Rabiner, L. R. (1989). A tutorial on hidden markov models and selected applications in speech recognition. *Proceedings of the IEEE 77*(2), 257–286.

[37] Moon, T. K. (1996). The expectation-maximization algorithm. *IEEE Signal processing magazine 13*(6), 47–60.

[38] Visser, I., M. Speekenbrink, et al. (2010). depmixs4: an r package for hidden markov models. *Journal of Statistical Software 36*(7), 1–21.

[39] Said, S. E. and D. A. Dickey (1984). Testing for unit roots in autoregressive-moving average models of unknown order. *Biometrika 71*(3), 599–607.

[40] Kwiatkowski, D., P. C. Phillips, P. Schmidt, and Y. Shin (1992). Testing the null hypothesis of stationarity against the alternative of a unit root: How sure are we that economic time series have a unit root? *Journal of econometrics 54*(1-3), 159–178.

[41] Bhansali, R. J. and P. S. Kokoszka (2001). Estimation of the long-memory parameter: a review of recent developments and an extension. *Lecture Notes-Monograph Series*, 125–150.

[42] Ljung, G. M. and G. E. Box (1978). On a measure of lack of fit in time series models. *Biometrika 65*(2), 297–303.

[43] McLeod, A. I. and W. K. Li (1983). Diagnostic checking arma time series models using squared-residual autocorrelations. *Journal of time series analysis 4*(4), 269–273.

[44] Lee, J. H. (1991). A lagrange multiplier test for garch models. *Economics Letters 37*(3), 265–271.

[45] Conover, W. J. and W. J. Conover (1980). Practical nonparametric statistics.